PCCP

Cite this: *Phys. Chem. Chem. Phys.*, 2012, **14**, 7076–7089

www.rsc.org/pccp

PAPER

Photodissociation dynamics of *tert*-butylnitrite following excitation to the S_1 and S_2 states. A study by velocity-map ion-imaging and 3D-REMPI spectroscopy†

Andreas M. Wenge,‡ Andreas Schmaunz, Uwe Kensy and Bernhard Dick*

Received 5th February 2012, Accepted 19th March 2012
DOI: 10.1039/c2cp40349h

Excitation of *tert*-butylnitrite into the first and second UV absorption bands leads to efficient dissociation into the fragment radicals NO and *tert*-butoxy in their electronic ground states $^2\Pi$ and ^2E, respectively. Velocity distributions and angular anisotropies for the NO fragment in several hundred rotational and vibrational quantum states were obtained by velocity-map imaging and the recently developed 3D-REMPI method. Excitation into the well resolved vibronic progression bands ($k = 0, 1, 2$) of the NO stretch mode in the $S_1 \leftarrow S_0$ transition produces NO fragments mostly in the vibrational state with $v = k$, with smaller fractions in $v = k - 1$ and $v = k - 2$. It is concluded that dissociation occurs on the purely repulsive PES of S_1 without barrier. All velocity distributions from photolysis *via* the $S_1(n\pi^*)$ state are monomodal and show high negative anisotropy ($\beta \approx -1$). The rotational distributions peak near $j = 30.5$ irrespective of the vibronic state $S_1(k)$ excited and the vibrational state v of the NO fragment. On average 46% of the excess energy is converted to kinetic energy, 23% and 31% remain as internal energy in the NO fragment and the *t*-BuO radical, respectively. Photolysis *via* excitation into the $S_2 \leftarrow S_0$ transition at 227 nm yields NO fragments with about equal populations in $v = 0$ and $v = 1$. The rotational distributions have a single maximum near $j = 59.5$. The velocity distributions are monomodal with positive anisotropy $\beta \approx 0.8$. The average fractions of the excess energy distributed into translation, internal energy of NO, and internal energy of *t*-BuO are 39%, 23%, and 38%, respectively. In all cases $\sim$8500 cm^{-1} of energy remain in the internal degrees of freedom of the *t*-BuO fragment. This is mostly assigned to rotational energy. An *ab initio* calculation of the dynamic reaction path shows that not only the NO fragment but also the *t*-BuO fragment gain large angular momentum during dissociation on the purely repulsive potential energy surface of S_2.

1 Introduction

Alkyl nitrites R–O–N=O show efficient photodissociation into RO and NO radicals following excitation to the first excited singlet state. Since the NO radicals are easily probed by laser excitation, alkyl nitrites have become prototype systems for the study of photodissociation dynamics of molecules that lead to molecular (as opposed to atomic) fragments. Laser induced fluorescence (LIF) or resonance enhanced multiphoton ionization (REMPI) can be used to obtain the populations of the rovibrational levels of the NO product states. Polarization experiments yield information on the alignment of angular momenta, and spectra with sub-Doppler resolution provide insight into the velocity distributions. By application of these techniques a wealth of information has been gathered on the photodissociation dynamics of alkyl nitrites, in particular for methyl nitrite CH_3ONO[1–8] and *t*-BuONO.[8–19] Reviews of this earlier work can be found in ref. 20 and 21.

In spite of this there are two good reasons for further studies on this class of compounds. First, just due to the large amount of information gathered so far there have emerged some questions that are still controversial. Secondly, these systems provide an excellent opportunity to demonstrate the power of new methods by comparing the results with those of earlier studies. In this article we present results obtained with the recently developed 3D-REMPI method,[22,23] which yields velocity distributions and anisotropies for many hundred rovibrational product channels of the photodissociation. This information was previously not accessible with reasonable experimental

Institut für Physikalische und Theoretische Chemie, Universität Regensburg, 93053 Regensburg, Germany. E-mail: bernhard.dick@chemie.uni-regensburg.de
† Electronic supplementary information (ESI) available. See DOI: 10.1039/c2cp40349h
‡ Present address: School of Chemistry, University of Bristol, Bristol BS8 1TS, UK. E-mail: Andreas.Wenge@bristol.ac.uk

effort. *I.e.* information on velocity distributions from the photolysis of alkyl nitrites exists only for few rovibrational states of NO, and only with methods of inferior resolution or sensitivity.

Before we present these new results and discuss their implications for controversial or yet open questions we should summarize what is already known. The vast majority of previous studies is concerned with the population of various quantum states of the NO product. With photolysis energies up to *ca.* 51 800 cm^{-1} (*i.e.* 193 nm) only NO fragments in the electronic ground state $^2\Pi$ have been observed, with similar populations in the two spin–orbit substates. Rotational state distributions were always non-statistical, usually well described by Gaussians that peak at $J \approx 35$[9,15] for photolysis *via* the S_1 state, and at $J \approx 55$ for photolysis *via* the S_2 state.[13] Bimodal distributions were reported in several studies and assigned to either clusters[14,15] or a second dissociation channel.[18] A few studies have been performed on the populations of the Λ-doublet states.[10,12] Polarization experiments indicate positive alignment of the angular momentum vector ($0.31 \leq A_0^{(2)} \leq 0.59$)[10,12,14,24] after photolysis from the S_1 state, and negative alignment ($A_0^{(2)} \approx -0.3$) after photolysis from the S_2 state.[12,25] Together these studies indicate that the NO fragment is rotating in the original CONO plane. When photolysis occurs from S_1, the unpaired electron preferentially resides in an orbital that is antisymmetric with respect to reflection at this plane.

In contrast to the effort invested into the quantum state distributions of NO, comparatively little is known about the velocity distributions resulting from photodissociation of alkyl nitrites. Early experiments with time-of-flight (TOF) methods found that the average kinetic energy amounts to *ca.* 40% of the excess energy for dissociation from the S_1 state.[13,26] However, these measurements average over all quantum states of the NO fragment. Data for specific quantum states following dissociation of jet-cooled nitrites were later obtained by the analysis of Doppler profiles.[12,14,25] A complete analysis *via* Doppler profiles requires measurements with different propagation directions of photolysis and probe beams. The profiles must be deconvoluted with the laser line width, and usually only monomodal velocity distributions were fitted. With the development of velocity map imaging (VMI) *ca.* 15 years ago,[27,28] velocity distributions can now be measured with much more precision and independently from the laser resolution. The photofragments are ionized by a REMPI process and subsequently accelerated by a static electric field towards an image detector (multichannel plate). The position at which the ion hits this detector measures the component of its velocity vector parallel to the detector surface. Analysis of these ion images yields velocity distributions and anisotropies. The VMI method is not limited by the laser bandwidth, and it can easily distinguish fragments in the same final quantum state that are produced by different dissociation channels associated with different velocities and anisotropies. Recently we have extended this method by combining the position sensitive detection with a scan over all REMPI resonances of the system.[22,23] In this way we obtain relative populations as well as velocities and anisotropies for several hundred quantum states of the NO fragment. This wealth of information was previously not available for photodissociations of alkyl nitrites. We present these data here since they not only complete our picture of the dissociation dynamics of this class of compounds. They also shed some light on still open questions regarding the mechanism of photodissociation from the S_1 state, as will be outlined below.

As a result of the earlier studies the following picture of photodissociation processes in alkyl nitrites has emerged: all these compounds dissociate with high efficiency after excitation to the first excited singlet state S_1. This state has been assigned nπ* character on the basis of the low absorption cross section ($\varepsilon \approx 200$ L mol^{-1} cm^{-1})[29] and has been assigned to the A″ representation of the C_S point group for the CONO frame.[10,30,31] Dissociation experiments in static electric fields showed that the transition moment for the $S_1 \leftarrow S_0$ excitation is perpendicular to the static dipole moment.[19] Since the latter is in the CONO plane of the molecule, this confirms the $n\pi^*$ assignment for the S_1 state. The absorption band of the $S_1 \leftarrow S_0$ transition shows a long progression in a vibration of *ca.* 1065 cm^{-1}. In the spectrum of *t*-BuONO, shown in Fig. 1, pronounced maxima up to a vibrational quantum number of $k = 5$ are clearly visible. In this case the electronic origin band ($k = 0$) peaks at 399 nm. The corresponding transition of MeONO is found at 388 nm. This vibration has been assigned to the N=O stretch mode in the S_1 state.[19] Experiments performed with MeONO have led to the conclusion that the preferred vibrational quantum number v in the NO fragment produced by dissociation following excitation to the progression member k is one less than the excited quantum number.[15] Such a propensity for $v = k - 1$ would indicate a vibrational predissociation mechanism. Similar conclusions have been drawn from lifetimes for the S_1 states of MeONO (125 ± 50 fs) and *t*-BuONO (130 ± 20 fs).[16] These lifetimes were obtained by pump–probe measurements on samples in a bulb at room temperature. It is concluded that, in order to overcome a barrier on the excited state potential energy surface (PES), one quantum in the NO stretch vibration must be converted to energy in the dissociation coordinate. Farmanara *et al.* reported characteristic times for the appearance of certain NO fragments from 350 nm photolysis of MeONO by analysis of

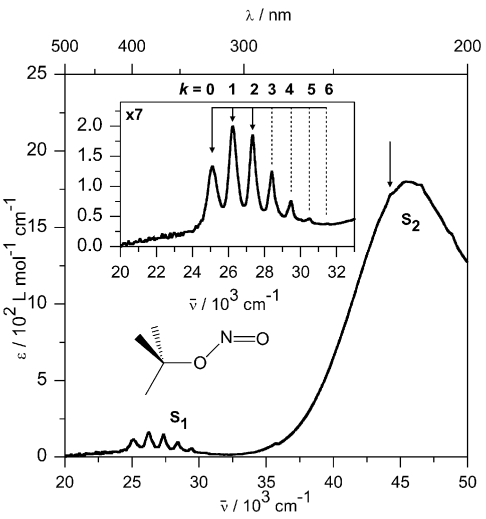

Fig. 1 Gas phase UV spectrum of *t*-BuONO. Arrows indicate the photolysis wavelengths applied in this study.

the anisotropy of the velocity distribution. They report $\tau = 320 \pm 100$ fs for NO($v = 0$), $\tau = 120 \pm 50$ fs for NO($v = 1$), and $\tau < 50$ fs for NO($v = 2$).[32] Since MeONO is excited to the progression member $k = 2$ at 350 nm, the observation of very fast production of NO with $v = 2$ would speak against a vibrational predissociation. This mechanism has also been questioned on the basis of photolysis experiments performed on MeONO in argon matrices.[33]

Most photodissociation experiments on MeONO in the gas phase have used a fixed photolysis wavelength of 355 nm (*i.e.* the third harmonic of the Nd:YAG laser), which is resonant with the $k = 2$ member of the vibrational progression. However, it should be considered that MeONO exists in two conformers, with *syn* and *anti* configuration of the CONO chain, respectively. At room temperature these conformers are populated with a ratio of *syn* : *anti* of 2 : 1,[34,35] and this ratio is apparently preserved during rapid cooling due to the rather high barrier for interconversion.[36] The original analysis of the gas phase absorption spectrum by Tarte[30] assigned only a small shift for the two electronic origins of both species. Thus progression bands of both conformers with the same value of k should overlap, and excitation into any of these bands should produce excited *syn* and *anti* species with the same vibrational excitation. Matrix isolation experiments, however, showed that the electronic origin ($k = 0$) of the *syn* species coincides almost perfectly with the band labeled $k = 1$ of the *anti* form.[33] If this assignment also applies to the gas phase, excitation at 355 nm would excite *anti* MeONO into $k = 2$, but *syn* MeONO into $k = 1$. Since a high yield of NO fragments with $v = 1$ is observed, a direct dissociation on a purely repulsive PES not involving a barrier would be a valid interpretation of the results. Two papers report dissociation of MeONO performed by excitation into the longest wavelength band.[37,38] The authors assume that they excite *syn* and *anti* MeONO at 380 nm and 388 nm, respectively, into the $k = 0$ state. If the assignment obtained from the matrix experiment[33] is correct, only *anti*-MeONO would be excited to $k = 0$ at these wavelengths. Nevertheless, both studies report efficient dissociation leading to NO in the vibrational ground state. Also, the large width of these absorption bands is at variance with the long lifetime expected for tunneling through a substantial barrier. If the proposed barrier exists on the PES of the S_1 state, it must be low enough so that it can be efficiently overcome by tunneling. *t*-BuONO offers a better opportunity for the study of this question, since the *syn* form is disfavored by steric effects and should occur only as a minor species at room temperature. From IR spectra a *syn* : *anti* ratio of less than 1 : 35 has been estimated.[30] We know of only one paper which reports on photolysis experiments of *t*-BuONO with excitation into the electronic origin of the S_1 absorption band, *i.e.* into the $k = 0$ progression member.[15] The product yield spectra reported in this paper show quite a substantial yield of NO in $v = 0$. Also, for excitation into $k = 1$ and $k = 2$ the yield of NO($v = k$) is greater or comparable to the yield of NO($v = k - 1$). These findings do not support a proposal for a barrier for photodissociation of *t*-BuONO on the S_1 PES.

Cooling in a supersonic jet can easily yield clusters of nitrites.[15] Photodissociation from clusters can lead to a second contribution to the rotational distribution for the NO fragments with a peak at much lower rotational quantum states than photodissociation of isolated molecules. Previous authors have relied on the assumption that this cluster formation has a sharp threshold in the stagnation pressure and occurs only at $p_S > 1850$ mbar.[18,19] Hence, they performed their experiments at $p_S \approx 1600$ mbar. We, however, find signatures of cluster formation in the velocity distribution which only vanish at stagnation pressures below 500 mbar in a He/Ne expansion, or at the very onset of the gas pulse. When we performed our experiments under conditions where no clusters are present in the beam, only monomodal rotational distributions for the NO fragments are observed. We conclude that all dissociation channels previously reported with a rotational distribution peaking at low rotational quantum numbers are in fact artifacts originating from the photodissociation of molecular clusters.

Although VMI has been developed more than one decade ago, most applications have dealt with atomic fragments, and applications on diatomic and larger fragments are only emerging in recent years. In 2004, Torsten Obernhuber performed VMI measurements on photolysis of *t*-BuONO *via* S_2. These data are presented in his PhD thesis[39] but were not published otherwise since we could not unambiguously separate contributions from monomers and clusters. To the best of our knowledge this study is the first report on VMI experiments performed with alkyl nitrites. In combination with the recently developed 3D-REMPI method we were able to measure the velocity distributions and relative populations of hundreds of rovibrational dissociation channels. Although much is already known about the photodissociation dynamics of alkyl nitrites, the present paper reports new information that complements and, to some extent, also corrects the picture that has emerged from previous studies.

2 Experimental

2.1 Materials

tert-Butylnitrite was obtained from Fluka (purity > 90% (GC)) and used without further purification. The purity was checked by UV–Vis and IR spectroscopy. Gas phase UV-spectra (Fig. 1) were measured using a UV-1800 (Shimadzu) spectrophotometer with the sample in a 10 cm long quartz cell under its own vapor pressure at room temperature (241 mbar[40]). *t*-BuONO was seeded into the supersonic jet by passing a mixture of helium and neon (70/30, Linde) at a pressure of 0.5 bar through a flask containing liquid *t*-BuONO cooled to −5 °C.

2.2 Apparatus

The VMI apparatus is a new construction which includes several components of our previous apparatus.[41] It consists of three vacuum chambers for supersonic jet creation, photolysis and ionization, and a field free drift region with the velocity analyzer. The gas mixture is expanded through a pulsed nozzle (General Valve No. 9, operated at 10 Hz) into a cylindrical stainless steel chamber pumped to a final pressure of 10^{-7} mbar by a combination of an oil diffusion pump (DI 3000, BOC Edwards) with water cooled oil baffle (DN250 ISO-K, Leybold), a mechanical booster (EH250, BOC Edwards), and a rotary pump (E2M40, BOC Edwards). The beam is then collimated by a skimmer (Beam Dynamics, 2 mm diameter)

and enters the photolysis and ionization chamber, pumped with a turbomolecular pump (EXT 255H, BOC Edwards) to a final pressure of 10^{-7} mbar. The molecular beam enters the photolysis and ionization region through a hole of 5 mm diameter in the repeller electrode. Two laser beams are used to photolyze the sample and ionize the fragments at the center between the repeller and the extractor electrodes. These laser beams are aligned counterpropagating and perpendicular to the molecular beam axis. The design of the ion optics was inspired by a similar one published in ref. 42 and was optimized with the SIMION software. The ions are accelerated towards a drift region of 484 mm length, pumped by a turbomolecular pump (EXT 70H, Edwards). At the end of this drift tube the ions were registered by a Chevron type double multichannel plate (Proxitronic) attached to a phosphor screen (P43, 40 mm active diameter). The voltage on this multichannel plate can be gated in order to select a specific ion mass. As a special feature of this new design the assembly of nozzle, skimmer, and ion optics can be mechanically aligned to the center of the detector under operating conditions without changing the region for photolysis and ionization. A drawing of the design and details on the voltage optimization are given in the ESI.†

Every ion produces a light spot on the phosphor screen which is imaged by a lens system (Schneider-Kreuznach XENON 25/0.95) onto a CCD Camera (Imager 3 LS, 1280 × 1024 pixel, LaVision). After a preset number of laser shots the data on the CCD chip are read out, transferred to a computer, and analyzed in the event counting mode by a combination of commercial software (DaVis, LaVision) and a program written with LabView. The data are then stored either as a conventional ion image (VMI mode) or in the form of the two maps ($r - \lambda$ and $\alpha - \lambda$) of the new 3D-REMPI mode.[22,23] Here, r and α are the polar coordinates (distance and angle) of the position where the ion hits the MCP. The $r - \lambda$ map is the ion intensity as a function of the REMPI wavelength λ and the distance r from the center of the MCP. For each REMPI resonance the $r - \lambda$ map shows a stripe perpendicular to the λ-axis which contains the distribution of the velocity component parallel to the MCP surface. The corresponding stripe in the $\alpha - \lambda$ map contains the angular distribution. From these data the 3D velocity distribution can be extracted for all REMPI resonances, as described in the section on data analysis.

The laser system consists of two dye lasers (FL3002 and LPD3000, spectral width *ca.* 0.2 cm^{-1}), each pumped by a XeCl excimer laser (Lextra 200 and Lextra 100, Lambda Physik). These beams are focused by quartz lenses (f = 40 mm, Linos) onto the molecular beam. The laser used for photolysis is polarized perpendicular to the supersonic jet and in the plane of the image detector. The NO fragments are ionized by a one-color (1 + 1) REMPI process. Resonant excitation with pulses of *ca.* 100 μJ pulse energy from the frequency doubled dye laser (Coumarin 120, BBO) into the $A^2\Sigma^+ \leftarrow \tilde{X}^2\Pi_{1/2,3/2}$ transition near 225 nm resulted in the selection of particular quantum states for analysis. For conventional VMI experiments the ionization laser was scanned over the Doppler profile of the selected NO rotational transition to ensure that all velocity components were detected with equal probability. For the measurement of 3D-REMPI data this laser was scanned over the region 218–230 nm. This accounts for all rovibrational states of the NO product with detectable population, *i.e.* with vibrational quantum number $v \leq 3$ and rotational quantum numbers $j \leq 75.5$. The same laser was also used to excite *t*-BuONO into the second absorption band with maximum near 217 nm. This band is tentatively assigned to the $S_2 \leftarrow S_0$ transition of *t*-BuONO. Photolysis by excitation into the various vibronic bands of the $S_1 \leftarrow S_0$ transition of *t*-BuONO in the range 400–360 nm was achieved with pulses of *ca.* 1 mJ pulse energy of the second dye laser. When both lasers were used, a temporal delay of 100 ns was applied between the photolysis and ionization laser pulses. Also, the diameter of the probe laser was chosen slightly larger than that of the dissociation laser. This avoids artifacts due to mixed two-color REMPI processes and ensures that the complete cloud of fragments is inside the ionization volume. The measurement of a complete ion image needed between 9000 and 72 000 laser shots. Since in the case of dissociation from the S_1 state the ionization laser can also dissociate the *t*-BuONO, the intensity was reduced as much as possible. The events caused by the ionization laser alone were subtracted by alternating measurements (5 laser shots each) with one laser only or with both lasers.

2.3 Data analysis

The ion image is the Abel transform of the three-dimensional velocity distribution of the fragments.[43] Several methods have been developed for reconstruction of the velocity distribution by numerical Abel inversion.[44–51] Since Abel inversion is a classical ill-posed problem, its application to noisy data can lead to artifacts that become especially large in the center of the image. Since the forward Abel transform is numerically stable, we prefer to analyze our data by a fit with a model function. The velocity distribution $P(v, \theta)$ resulting from dissociation following a non-saturated one-photon excitation with linearly polarized light can be written in the general form

$$P(v, \theta) = P(v)[1 + \beta(v)\mathscr{P}_2(\cos\theta)] \quad (1)$$

where $\mathscr{P}_2$ is the second Legendre polynomial, v is the modulus of the velocity, and θ is the angle between the velocity vector and the polarization direction of the photolysis light. In this general expression the anisotropy parameter $\beta(v)$ is a function of the velocity. The velocity distribution averaged over all angles is given by $Q(v) = v^2P(v)$. We observed that a sum of Gaussian functions $p_i(v)$, each associated with a constant anisotropy parameter β_i, is a good approximation to eqn (1). *I.e.*, we use the fit function

$$P(v,\theta) = \sum_i \hat{p}_i(v,\theta) = \sum_i p_i(v)[1 + \beta_i\mathscr{P}_2(\cos\theta)] \quad (2)$$

with

$$p_i(v) = A_i \exp\left(-\frac{(v - v_i)^2}{2\sigma_i^2}\right) \quad (3)$$

The population N_i in this velocity distribution is determined through the parameters $A_i v_i$, and σ_i by

$$N_i = A_i\sigma_i^2 v_i \exp\left(-\frac{v_i^2}{2\sigma_i^2}\right) + A_i\sigma_i\sqrt{\frac{\pi}{2}}(v_i^2 + \sigma_i^2)\left(\mathrm{erf}\left(\frac{v_i}{\sigma_i\sqrt{2}}\right) + 1\right) \quad (4)$$

We have observed previously[23,41,52] that these fits are in good agreement with the result of a direct Abel inversion by the matrix method[53] when the signal to noise ratio is high. When several dissociation channels contribute, the fitting approach yields a separate anisotropy parameter for each channel.

The 3D-REMPI method and the global fit technique used for the analysis of the 3D-REMPI data have been outlined in ref. 22 and 23. The velocity distribution for every rovibrational state of NO(v, j, Ω) and for each dissociation channel is described by a function $\hat{p}_i(v, \theta)$ (eqn (2)), where $p_i(v)$ is given by eqn (3). The contribution of such a velocity distribution to the two maps ($r - \lambda$ and $\alpha - \lambda$) is given by a transformation similar to the Abel transform. A global fit of this transformed function to a $r - \lambda$ map from a 3D-REMPI experiment yields four parameters (N_i, v_i, σ_i, β_i) for each of several hundred quantum states j of the NO fragments simultaneously. When the laser bandwidth and the Doppler width of the REMPI transition are of similar size, the pattern produced by each transition in the $r - \lambda$ map is not sensitive to the value of β. Therefore, β was obtained from analysis of the $\alpha - \lambda$ map.

Each rovibrational quantum state of NO contributes to 6 branches in the REMPI spectrum. However, every transition frequency of the two Q-branches is very close to either one in a P-branch or a R-branch. With our laser bandwidth thus only four branches can be resolved. This means that the parameter set (N_i, v_i, σ_i, β_i) for each quantum state is determined with fourfold redundancy by the global fit. As a consequence, the information contained in regions of the 3D-REMPI spectra which are congested (*e.g.* near the band heads) or overlap with signals from contaminations (*e.g.* due to thermally produced NO) can be obtained from other parts of the data set.

2.4 Quantum chemical calculations

Electronic structure calculations were performed with the GAMESS[54] quantum chemical program package, in particular with the PCGAMESS[55] version optimized for Intel processors and Windows operation system. The ground state structures of *t*-BuONO and the fragments NO and *t*-BuO were optimized with density functional theory (DFT) employing the B3LYP[56–58] functional. Energies and vibrational frequencies at these geometries provide the dissociation energy with correction for the zero point vibrational energy (ZPE). The basis set superposition errors (BSSE) were corrected by the counterpoise method.[59] Vertical electronic excitation energies for closed shell systems were calculated with the TD-DFT method. For all calculations involving electronically excited states and their comparison with the ground state CASSCF type wavefunctions were used in order to ensure that the results for different electronic states are of comparable quality.

3 Results and analysis

3.1 Calculations

Three basis sets were used: cc-pVDZ, aug-cc-pVDZ, and aug-cc-pVTZ.[60] These are abbreviated in the following as CCD, ACCD, and ACCT, respectively. The ACCD basis adds diffuse functions to the CCD basis. Thus it can account for Rydberg states that might occur in the energetic region of the second UV absorption band. The ACCT basis extends the flexibility of the ACCD basis from double-ζ to triple-ζ. A comparison of the results obtained with basis sets of increasing flexibility and size allows an estimate to what extent the numbers have converged towards the exact values. The detailed results obtained with all three basis sets are collected in the ESI.†

3.1.1 *Syn* and *anti* forms. For several alkyl nitrites it has been found that the CONO chain can exist in two conformers known as *syn* or *anti* forms. Both structures may be minima on the PES of the electronic ground state, but the relative energetic ordering depends on the steric requirements of the alkyl group. In the case of methyl nitrite, CH_3ONO, the *syn* form is the global minimum, but the energy of the *anti* form is only slightly higher so that both forms coexist at room temperature in a 2 : 1 ratio. Due to a rather high barrier for rotation this ratio is also trapped when CH_3ONO is isolated in rare gas matrices.[36] In the case of *t*-BuONO the *anti* form has been proposed as the global minimum, but a small amount of the *syn* form has also been proposed based on the analysis of IR spectra in the region of the NO stretch frequency.[61] Our data that will be discussed later are in good agreement with the assumption that only one species is present in the molecular beam. In order to estimate their relative energies we optimized the structures of both isomers with the DFT/B3LYP method. With all three basis sets the *anti* isomer is found with the lower energy. The energy difference, including correction for the zero point vibrational energy (ZPE), increases from 631 cm^{-1} (CCD) to 1175 cm^{-1} (ACCD) and 1222 cm^{-1} (ACCT) with increasing size of the basis set. We conclude that the two isomers are separated by more than 1200 cm^{-1} in energy, and that hence at room temperature less than 2% of the *t*-BuONO is in the *syn* form. This is in good agreement with an early estimate based on spectroscopic data.[30]

3.1.2 Excitation energies. Vertical excitation energies were calculated with the TD-DFT/B3LYP method. The first excitation is found to be a $n\pi^*$ transition in the spectral range 26 200–26 650 cm^{-1} for the *anti* form and 27 530–27 920 cm^{-1} for the *syn* form. In both cases the excitation energy increases slightly with increasing size of the basis set. Table 1 shows the results obtained with the ACCT basis. The observed maximum of the Franck–Condon progression at 26 200 cm^{-1} (see Fig. 1) is in very good agreement with the calculated vertical excitation energy for the *anti* isomer. The second excitation energy corresponds to a $\pi\pi^*$ transition, calculated at 45 800 cm^{-1} for the *anti* form and at 48 000 cm^{-1} for the *syn* form. Again the observed excitation energy of 45 500 cm^{-1} is in good agreement with the value calculated for the *anti* isomer. Interestingly, inclusion of diffuse basis functions did not lead to Rydberg states below 50 000 cm^{-1}. To name a counter example, Rydberg states were observed in the case of *N*-nitrosopyrrolidine, thus giving some ambivalence to the assignment of the strong UV absorption band.[52] In the present case of *t*-BuONO, however, contributions of Rydberg states to the strong UV absorption band with maximum at 220 nm are very unlikely. Hence, we attribute this absorption band to the $S_2 \leftarrow S_0$ transition.

3.1.3 Dissociation energies. The dissociation energy of *t*-BuONO into a NO fragment and a *t*-BuO radical was

Table 1 Excitation energies and oscillator strengths of the lowest 10 transitions of the *syn* and *anti* forms of *t*-BuONO calculated by TD-DFT/aug-cc-pVTZ

State	ΔE/eV	$\Delta\nu$/cm^{-1}	λ/nm	f
	syn t-BuONO			
1A″	3.4615	27 919	358.18	0.0012
2A″	5.9676	48 132	207.76	0.0001
2A′	6.0074	48 453	206.39	0.0367
3A′	6.4343	51 896	192.69	0.0243
3A″	6.8270	55 064	181.61	0.0001
4A′	6.9976	56 440	177.18	0.0201
4A″	6.9984	56 446	177.16	0.0031
5A′	7.0836	57 133	175.03	0.0171
6A′	7.1498	57 667	173.41	0.0215
7A′	7.4826	60 351	165.70	0.0086
	anti t-BuONO			
1A″	3.3047	26 654	375.18	0.0010
2A′	5.6850	45 853	218.09	0.0596
2A″	6.1626	49 705	201.19	0.0004
3A′	6.3692	51 371	194.66	0.0122
3A″	6.8151	54 967	181.93	0.0003
4A′	6.9124	55 752	179.36	0.0062
4A″	6.9399	55 974	178.65	0.0031
5A′	7.0368	56 755	176.20	0.0076
6A′	7.0964	57 237	174.71	0.0207
7A′	7.4214	59 858	167.06	0.0023

calculated with the DFT/B3LYP method. The electronic dissociation energy increased with increasing size of the basis set from 13 456 cm^{-1} (CCD) over 13 980 cm^{-1} (ACCD) to 14 111 cm^{-1} (ACCT). The BSSE correction decreased in the same order, amounting to only 104 cm^{-1} with the ACCT basis. Extrapolation to zero BSSE resulted in an electronic dissociation energy of 14 176 cm^{-1}, which is reduced to 12 909 cm^{-1} by considering the zero point vibrational energies (obtained with the ACCT basis).

3.1.4 Excitation energy of the *t*-BuO radical. In order to estimate whether the *t*-BuO radical might be produced in an electronically excited state the structure of this radical was optimized in the ground and first excited states. The ground state of *t*-BuO belongs to the irreducible representation E in the idealized point group C_{3v} and undergoes a Jahn–Teller splitting and symmetry reduction to the C_S point group upon geometry optimization. In order to treat all states with equivalent wave functions optimization was not performed with the DFT method but with MCSCF. An active space of 5 electrons in 3 orbitals was employed, accounting for all non-bonding electrons of the oxygen atom. CASPT2 calculations at the optimized geometries were used to account for dynamic correlation. This resulted in a Jahn–Teller splitting of the optimized ground state structures of 130 cm^{-1}, and an energy difference of the two lowest optimized structures of A' symmetry of 26 032 cm^{-1}. We conclude that *t*-BuO fragments with an internal energy below *ca.* 25 000 cm^{-1} are produced in their electronic ground states.

3.2 Separation of clusters from monomers

Alkyl nitrites show a substantial interaction energy in the gas phase and have a strong tendency to form aggregates in a supersonic jet. This has been concluded from the observation of bimodal distributions of the rotational population in the NO photodissociation products.[14,15] However, in a later publication such bimodal rotational distributions have been linked to a second decay channel employing a linear O–NO transition state on the excited state potential energy surface.[18]

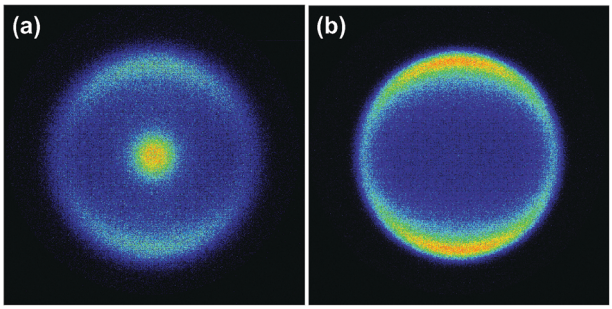

Fig. 2 Ion images measured for NO(Ω = 3/2, v = 0, j = 48.5) produced by photolysis *via* the S_2 state of *t*-BuONO. (a) Measurement at τ_D = 190 μs after the beginning of the gas pulse. (b) Measurement at the rising edge of the gas pulse (τ_D = 0 μs). The stagnation pressure was p_S = 1.5 bar. Here and in all subsequent false color plots the intensity increases in the sequence blue, green, yellow and red.

If the ion signal has contributions from monomers and clusters, the relative magnitude of these contributions should depend on the expansion conditions of the supersonic beam. Hence we studied carefully the influence of the stagnation pressure p_S and the delay time τ_D between the beginning of the gas pulse and the photolysis laser on the ion images of selected rotational states of the NO fragment. A typical ion image for p_S = 1.5 bar and τ_D = 190 μs is shown in Fig. 2(a). Photolysis was performed at 224.902 nm by excitation to the S_2 state. The REMPI laser was set to ionize NO fragments in the $^2\Pi_{3/2}(v = 0, j = 48.5)$ state. Due to the high rotational excitation the signal cannot have contributions from cold NO fragments formed by thermal decomposition of *t*-BuONO in the nozzle. The image shows a ring with positive anisotropy (β = 0.7) corresponding to fragments with a velocity of *ca.* 2670 m s^{-1}, and a center spot with low anisotropy ($\beta \approx 0$) and velocity $v < 612$ m s^{-1}. When the measurement is performed right at the beginning of the gas pulse (τ_D = 0), only the first component is seen, while the spot in the center of the image is missing (see Fig. 2(b)). The fraction of ions in the center spot increases with increasing stagnation pressure and has a maximum at delay times of *ca.* 200 μs. For high rotational quantum numbers the center spot always disappears completely at the beginning of the gas pulse (τ_D = 0). For fragments with low rotational quantum numbers the center spot can sometimes be observed even at τ_D = 0, however never at stagnation pressures below 0.5 bar.

Obviously, two species contribute to the signal: one yields fast fragments with large anisotropy, the other slow fragments with low anisotropy. This second species is not present in the beam when the stagnation pressure is lower than 0.5 bar or the measurement is performed at the rising edge of the gas pulse. These observations are consistent with the assignment of the first component to *t*-BuONO monomers, and of the second component to *t*-BuONO clusters. The fraction of clusters should increase with increasing stagnation pressure since this results in better cooling of the supersonic jet. Also, due to the velocity slip experienced by larger masses,[62] clusters should appear later in the gas pulse than the monomers. The production

of fragments with small velocities and anisotropies by photodissociation of clusters can be rationalized in several ways. Fragments produced by photodissociation of a molecule inside a cluster will lose much of their kinetic and rotational energy by collisions before they can leave the cluster. These collisions will also destroy the correlation between the initial orientation of the transition dipole and the final velocity vector. This correlation is also lost when the initially excited molecule transfers the excitation energy to a neighbor in the cluster which subsequently dissociates. Repeated energy transfer between molecules in the cluster can delay the photodissociation, making the velocity distribution more isotropic. Fragments produced by dissociation of molecules at the surface of clusters will be less influenced by these effects and can contribute to the signals in the ion image near those of the fragments from isolated molecules. In fact we observe a broadening of the velocity distribution attributed to the monomer dissociation under conditions which favor cluster production. The width (FWHM) of the faster velocity component in Fig. 2 increases from 33 m s^{-1} at p_S = 0.5 bar to 128 m s^{-1} at p_S = 1.5 bar. This broadening is accompanied by a decrease of the anisotropy. Therefore, in all experiments discussed later in this paper we used a stagnation pressure of 0.5 bar and performed the dissociation at the rising edge of the gas pulse. Under these conditions the velocity distribution of the fragments is always monomodal, narrow, and shows pronounced anisotropy. Under these conditions we also observe only monomodal distributions of the rotational quantum states. *I.e.*, the second contribution with maximum at small rotational quantum numbers reported in ref. 14, 15 and 18 is missing. This confirms the assignment of these product states to dissociation from clusters[14,15] and rules out the assignment to a second dissociation channel proposed in ref. 18.

3.3 Dissociation energy of *t*-BuONO

The dissociation energy D_0 of *t*-BuONO was estimated by application of the equation

$$D_0 = h\nu - E_{kin}^{(MAX)} - E_{int}(NO) \qquad (5)$$

where $h\nu$ is the energy of the photolysis photon, $E_{kin}^{(MAX)}$ is the maximum total kinetic energy release of the fragments, and E_{int}(NO) is the internal energy of the NO fragment selected by the specific REMPI transition. Eqn (5) is based on the assumption that the NO fragments with the largest kinetic energy correspond to *t*-BuO counter fragments with no internal energy. If this is not the case, the dissociation energy will be overestimated, and the value of D_0 obtained by use of eqn (5) must be regarded as an upper limit. $E_{kin}^{(MAX)}$ was chosen as the value at which the total kinetic energy distribution drops to 1% of its maximum. In this way an average of the dissociation energy of $D_0 \leq 15\,400 \pm 600$ cm^{-1} was obtained by analyzing 27 ion images for photolysis from S_1. This is *ca.* 8% higher than the value reported by Batt and Milne (14 308 ± 400 cm^{-1})[63] obtained by calorimetric measurements in the temperature range 120–190 K.

Our best theoretical estimate of the dissociation energy is 12 900 cm^{-1}, which is 1400 cm^{-1} lower than the value obtained by Batt and Milne.[63] If the value of Batt and Milne is correct, our method of using eqn (5) overestimates the dissociation energy by *ca.* 1100 cm^{-1}. If we take the calculated value for the true dissociation energy, our experimental estimate is 2500 cm^{-1} too high. Hence, we are led to the conclusion that an internal energy of *ca.* 1100–2500 cm^{-1} always remains in the counter fragment when dissociation occurs on the S_1 PES.

Applying eqn (5) to the dissociation from the S_2 state of *t*-BuONO results in an estimate of $D_0 \leq 22\,800 \pm 2800$ cm^{-1}, which is much too high. Based on the theoretical estimate given above this corresponds to a residual internal energy of the counter fragments of *ca.* 9900 cm^{-1}. If we take the value of Batt and Milne for the dissociation energy, the residual internal energy of the *t*-BuO fragment is *ca.* 8500 cm^{-1}. In a previous study on the photodissociation of *N*-nitrosopyrrolidine[52] a residual internal energy of similar size could be attributed to the fact that the counter fragment radical was produced in an electronically excited state. According to our CASPT2/aug-cc-pVTZ calculations, the optimized structure of the first electronically excited state of the *t*-BuO radical is *ca.* 26 000 cm^{-1} above the ground state. Hence, the residual internal energy, although rather large, cannot be accounted for by electronic excitation. It must therefore be attributed to rotational and probably also vibrational excitation of the *t*-BuO fragment.

3.4 Fragment yield spectra from S_1

With a small change in the data acquisition mode our apparatus permits the measurement of three-dimensional ion yield spectra (3D-IYS).[23] This is accomplished by fixing the ionization laser to a particular REMPI resonance and scanning the photolysis laser. Integration of all ions for each laser wavelength results in the ion yield spectrum (IYS) for the particular quantum state of the NO fragment selected by the REMPI transition. This IYS is proportional to the partial absorption cross section for this particular photodissociation channel. In a 3D-IYS the ions are integrated on the detector area in the same manner as in the $r - \lambda$ maps. As an example, Fig. 3 shows the 3D-IYS (a) and the *r*-integrated IYS (b) for

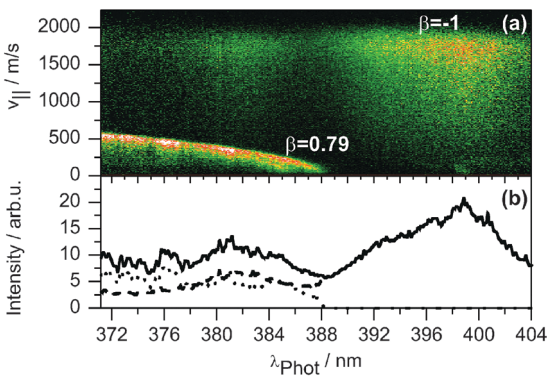

Fig. 3 Ion yield spectrum of the fragment NO(Ω = 1/2, v = 0, j = 19.5) monitored on the Q_{11}/P_{21} REMPI transition. (a) Velocity resolved 3D-IYS. Two contributions can be discerned. One has large velocities up to 2000 m s^{-1} with anisotropy $\beta = -1$. The second sets in at a threshold of 388.59 nm has small velocities ($v_\parallel < 500$ m s^{-1}) and positive anisotropy ($\beta = 0.79$). (b) IYS obtained by velocity integration of the 3D-IYS. The continuous curve is integrated over all data, whereas the dotted and dashed lines represent the velocity regions between $0 \leq v_\parallel < 500$ m s^{-1} and $v_\parallel > 500$ m s^{-1}.

the NO($\Omega = 1/2$, $v = 0$, $j = 19.5$) fragment detected on the $Q_{11} + P_{21}$ transition. The IYS reveals maxima at 399 nm and 381 nm. These wavelengths correspond to the maxima labeled $k = 0$ and $k = 1$ in the absorption spectrum. Hence, excitation of *t*-BuONO at these bands leads to NO in the vibrational ground state. Inspection of the 3D-IYS shows that these fragments have a velocity of *ca.* 2000 m s^{-1}, and the corresponding $\alpha - \lambda$ map (not shown) reveals strong negative anisotropy ($\beta = -1$) for these fragments. The 3D-IYS reveals an additional contribution that sets in at photolysis wavelengths $\lambda_P < 388.59$ nm. This threshold wavelength corresponds to an energy of 25 734 cm^{-1}. Since at this threshold no kinetic energy is released and the NO fragment has an internal energy of 608 cm^{-1}, an energy of 25 126 cm^{-1} is available for the dissociation energy and the internal energy of the counter fragment. With increasing photolysis energy the velocity increases proportional to the square root of the energy above the threshold. *I.e.*, the kinetic energy is proportional to the photolysis energy above threshold. For these fragments the $\alpha - \lambda$ map reveals positive anisotropy ($\beta = 0.79$). The energy available for dissociation at threshold is in very good agreement with the known dissociation energy of NO_2 of 25128.57 cm^{-1}.[64] This dissociation produces oxygen atoms in their ^3P electronic ground states. Hence, the second component in the 3D-IYS can be assigned to photolysis of NO_2, presumably produced by thermal decomposition of *t*-BuONO in the nozzle. The 3D-IYS nicely separates this contribution from that due to photodissociation of *t*-BuONO. The partial dissociation cross section of *t*-BuONO can easily be obtained from these data by excluding the region $v_{\parallel} < 550$ m s^{-1} from integration.

Fig. 4 shows 3D-IYS for several vibrational and rotational states of the NO fragment aligned to the same wavelength axis

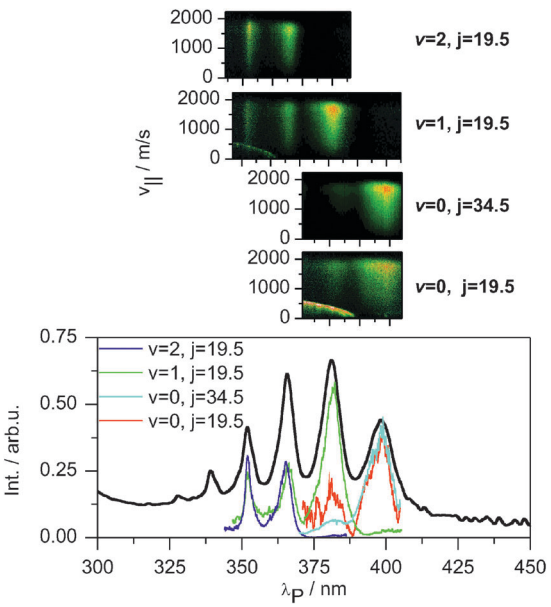

Fig. 4 3D-IYS and partial absorption spectra of the first absorption band of *t*-BuONO. The thick line represents the gas phase absorption spectrum (*cf.* Fig. 1). The colored lines show different partial absorption spectra, resulting from velocity integration (*i.e.* vertical binning) of the ion yield maps.

and in comparison to the absorption spectrum in the range of the $S_1 \leftarrow S_0$ absorption band of *t*-BuONO. The same integration times were used in all 3D-IYS, so the intensities can be compared. The lowest 3D-IYS for NO($v = 0$, $j = 19.5$) is the same as discussed above. The next 3D-IYS monitors also the vibrational ground state of NO, but a higher rotational state ($j = 34.5$). The third and fourth 3D-IYS monitor vibrationally excited NO with $v = 1$ and $v = 2$, respectively. The following conclusions can be drawn from these data: NO fragments with a particular vibrational excitation v are only observed upon excitation of the vibronic lines with $k \geq v$ in the absorption spectrum of *t*-BuONO. For excitation into a given absorption band k the largest fraction of NO fragments has vibrational excitation $k = v$. This is in contrast to a propensity for $v = k - 1$ proposed for methyl nitrite.[15] In *t*-BuONO the wavepacket in the NO stretch coordinate produced by excitation into a particular vibronic band k is apparently conserved, leading predominantly to NO fragments with the same vibrational excitation. Thus it is unlikely that the dissociation has to overcome a barrier along the dissociation coordinate. Such a barrier has been proposed in the case of methyl nitrite, and it has been argued that the energy of one vibrational quantum of the NO stretch has to be converted into energy along the dissociation coordinate in order to overcome this barrier. Obviously no such vibrational redistribution is required for dissociation in the case of *t*-BuONO. Hence, we conclude that dissociation is a very fast process and occurs on a purely repulsive potential energy surface. This conclusion is supported by the very low value of the anisotropy ($\beta \approx -1$) which requires two conditions: first, the transition dipole and the fragment velocity vectors must be perpendicular, which is naturally fulfilled if the electronic excitation is a $n\pi^*$ transition. Secondly, dissociation must occur on a time scale short compared to the rotational period of the parent molecule. The line shapes of the partial cross sections (IYS) shown in Fig. 4 are well fitted by Lorentzian lines of *ca.* 400 cm^{-1} widths. If these are interpreted as homogeneous line widths, the excited state lifetimes can be estimated in the range (14 ± 4) fs, which is definitely much shorter than typical rotational coherence times of molecules of this size.

3.5 VMI and 3D-REMPI data

3D-REMPI spectra have been measured for excitation into the first three vibronic bands ($k = 0$, 1, 2) of the $S_1 \leftarrow S_0$ transition of *t*-BuONO. The $r - \lambda$ map for $k = 1$ is shown in Fig. 5. The $r - \lambda$ map for $k = 0$ and $k = 2$ as well as the corresponding $\alpha - \lambda$ maps can be found in the ESI.† For 27 well isolated REMPI transitions conventional ion images were measured. These contain a much larger number of ions than the corresponding feature in the 3D-REMPI spectrum and thus allow for a more precise fit of the velocity model. An example of such an ion image is shown in Fig. 6. Each vertical line in the 3D-REMPI spectrum shown in Fig. 5 corresponds to a velocity distribution of a specific rovibrational state of the NO fragments. The upper end of each line marks the largest velocity component tangential to the detector surface, which is also the upper limit of the absolute value of the velocity. This is in the range 1700–2000 m s^{-1} for the fragments

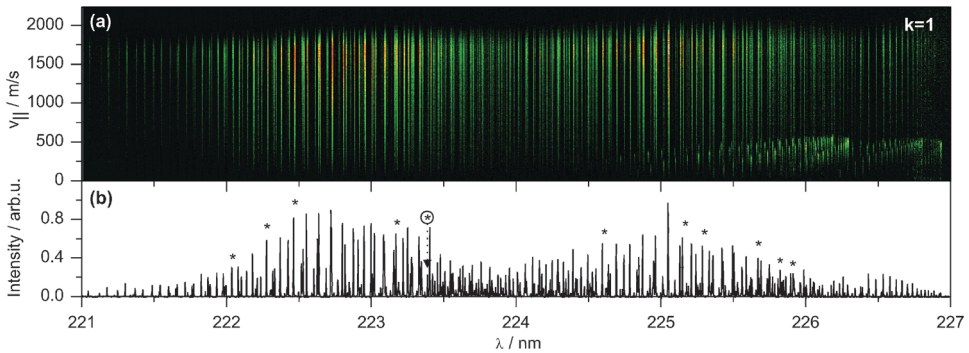

Fig. 5 (a) $r - \lambda$ map of the NO fragments produced by photolysis of *t*-BuONO *via* the $S_1(k = 1)$ state. (b) Conventional REMPI spectrum obtained by integration of the 3D-REMPI data along $v_{||}$. Asterisks mark transitions for which conventional ion images were measured.

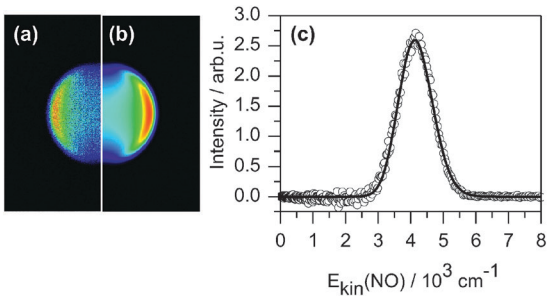

Fig. 6 (a) Ion image of NO($v = 1$, $j = 19.5$) resulting from the photodissociation of *t*-BuONO at 26 247 cm^{-1} ($k = 1$). The image was accumulated over 36 000 laser shots while scanning the Doppler profile of the Q_{11}/P_{21} REMPI transition (see encircled asterisk in Fig. 5). (b) Fitted image obtained by using one Gaussian velocity component (eqn (3)). (c) Kinetic energy distribution of the NO fragment. The full line is the fit, the points show the distribution obtained by Abel inversion with the matrix method followed by angular integration. The anisotropy parameter is $\beta = -1$.

from photodissociation of *t*-BuONO. A second set of lines ending at $v_{||} < 500$ m s^{-1} is due to the second component observed in Fig. 3(a) which has been assigned to photodissociation of NO_2.

A global fit to the 3D-REMPI data results in population distributions for all rotational and vibrational states of the NO fragment as well as their velocity distributions. The results of these fits are summarized in Fig. 7. The left column shows rotational distributions within the vibrational state indicated. Open symbols refer to the $^2\Pi_{3/2}$ state, full symbols to the $^2\Pi_{1/2}$ state. Both spin–orbit states are almost equally populated, in some cases a small preference for the $^2\Pi_{1/2}$ state seems to exist. All rotational distributions peak near $j = 30.5$. Table 2 presents the relative populations, integrated over all rotational states, for the vibrational states $v = 0$, 1, 2 produced after excitation to the progression bands $k = 0$, 1, 2. As already noted in the 3D-IYS (*i.e.* for a particular rotational state), the largest fraction of fragments occurs always for $v = k$. The right column of Fig. 7 shows the correlation of the kinetic energy with the internal energy of the NO fragment. Circles indicate the data from the 3D-REMPI spectra, triangles indicate the results from the analysis of the ion images. In all cases a linear relation is obtained, indicated by the dashed lines. With increasing internal energy of the NO fragment the

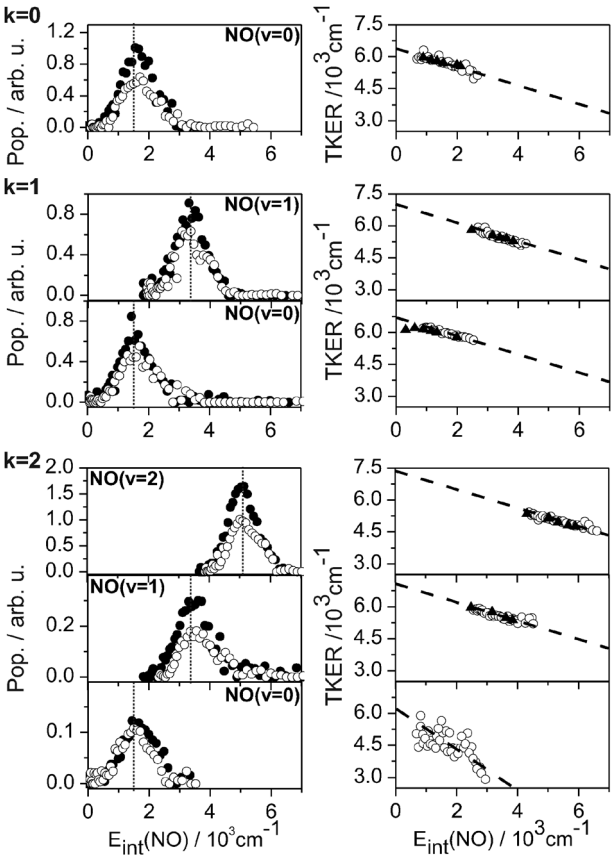

Fig. 7 Analysis of 3D-REMPI data for photolysis from S_1. The left column shows relative populations of rotational states plotted as a function of the total internal energy of the NO fragment. The vibrational band excited in *t*-BuONO ($k = 0$, 1, 2) is indicated at the upper left of each panel, the vibrational state of NO($v = 0$, 1, 2) monitored is indicated. Full symbols indicate populations of the $^2\Pi_{1/2}$ state, open symbols refer to the $^2\Pi_{3/2}$ state. In order to facilitate comparison of the rotational distributions, the position of the rotational states with $j = 30.5$ is indicated by a vertical dotted line. The right side shows, for each of the dissociation channels of the left side, the total kinetic energy release (TKER) as a function of the total internal energy of the NO fragments.

kinetic energy becomes smaller. The slope of the lines is near 0.3, indicating that *ca.* 30% of the increase in internal energy of the NO fragment is supplied from the kinetic energy, while

Table 2 Fractions of populations in the spin–orbit ($^2\Pi_\Omega$) and vibrational states ($v = 0, 1, 2$) of NO produced by excitation into the progression members ($k = 0, 1, 2$) in the $S_1 \leftarrow S_0$ absorption band

	$k = 0$	$k = 1$		$k = 2$		
Ω	$v = 0$	$v = 0$	$v = 1$	$v = 0$	$v = 1$	$v = 2$
$^2\Pi_{1/2}$	0.61	0.25	0.33	0.02	0.11	0.46
$^2\Pi_{3/2}$	0.39	0.21	0.21	0.02	0.06	0.33
Sum	1.00	0.46	0.54	0.04	0.17	0.79

the other 70% are supplied by the internal energy of the *t*-BuO counter fragments. On average, 46% of the excess energy of the photolysis is converted to kinetic energy, 23% is found as internal energy in the NO fragments, and the remaining 31% must be attributed to internal energy of the *t*-BuO fragments.

3.6 Photodissociation following excitation to the S_2 state

The photodissociation dynamics of *t*-BuONO following excitation to the S_2 state was studied by using the same laser to photolyze *t*-BuONO and to probe the NO products. As a consequence, the photolysis wavelength changes slightly during data acquisition. Fig. 8 shows the $r - \lambda$ map from the 3D-REMPI measurement and the conventional REMPI spectrum of the NO fragments produced by excitation of *t*-BuONO to the second absorption band. For several rovibronic transitions additional VMI measurements were performed. These transitions are marked with an asterisk in Fig. 8. A typical result of these VMI experiments is shown in Fig. 9, showing the data, the fit, and the resulting kinetic energy distribution for NO($\Omega = 3/2$, $v = 0$, $j = 48.5$). All ion images show positive anisotropy parameter $\beta \approx 1.0$ in agreement with the $\pi\pi^*$ character of the electronic excitation. For all quantum states of the NO fragment rather narrow velocity distributions are found, with a mean value of the width (FWHM) of $\Delta v = 149 \pm 13$ m s^{-1}.

Analysis of the 3D-REMPI spectra yields the rotational population distributions for NO shown in Fig. 10. The anisotropy parameters for NO fragments in the vibrational ground state, obtained from VMI and $\alpha - \lambda$ maps of 3D-REMPI experiments, are shown in Fig. 11. The anisotropy is positive throughout, slightly decaying from $\beta = 1.0$ for low rotational excitation to $\beta = 0.8$ for high rotational excitation. For all vibrational quantum states the rotational population distributions

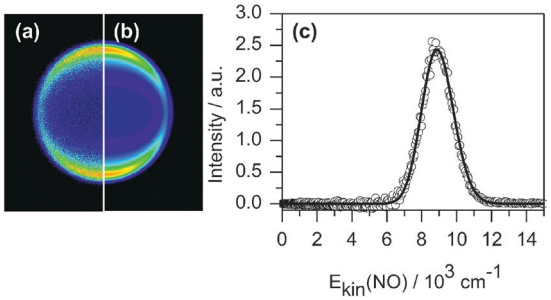

Fig. 9 (a) Ion image of NO($v = 0$, $j = 48.5$) resulting from the photodissociation of *t*-BuONO at 44 464 cm^{-1}. The image was accumulated over 17 000 laser shots while scanning the Doppler profile of the P_{12} REMPI transition. (b) Ion image obtained by a fit of one Gaussian velocity component. (c) Kinetic energy distribution of the NO fragment. The full line is the fit of one Gaussian component, the points show the distribution obtained by Abel inversion with the matrix method followed by angular integration. The anisotropy parameter is $\beta = 0.9$.

show a single peak with maximum near $j = 59.5$ and no significant population below $j = 45.5$. The spectral region chosen in the experiment contains redundant information for the first vibrationally excited state of NO($v = 1$). This is accessed by using either $v' = 1$ or $v' = 0$ as the intermediate state in the REMPI process. Comparison of the panels (b) and (c) in Fig. 10 shows that the integrals over the rotational population distribution for NO($v = 1$) obtained in these two ways differ by a factor of 4. This could be an artifact if in one of the two cases the resonant transition of the REMPI process were not saturated. However, we observe the same dependence of the signal on the laser power in both cases. A separate analysis of each of the four spectrally resolved rotational branches for a fixed intermediate vibrational level v' leads to very similar population distributions. Although ionization of the same initial state *via* different rotational branches in the REMPI process corresponds to small variations in the photolysis energy in the order of *ca.* 50 cm^{-1}, these variations have apparently no significant effect on the rotational distributions. We also note that the rotational distributions are rather similar for different vibrational levels v'' if the REMPI process uses a transition with $v'' = v'$. The significantly different result observed for $v' = v'' - 1$ corresponds to an excess energy which is lower by *ca.* 2340 cm^{-1} than for the

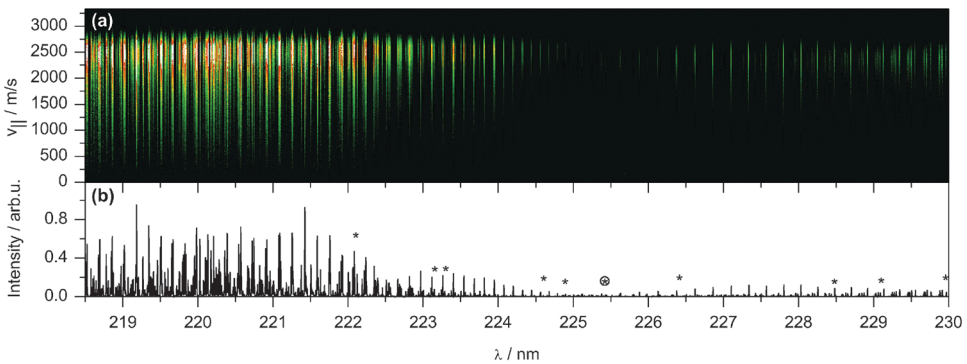

Fig. 8 3D-REMPI data from the photolysis *via* the S_2 state. The photolysis wavelength is identical to the probe wavelength. (a) The $r - \lambda$ map. (b) Conventional REMPI spectrum obtained by velocity integration of the $r - \lambda$ map. The asterisks indicate the transition where ion images are recorded.

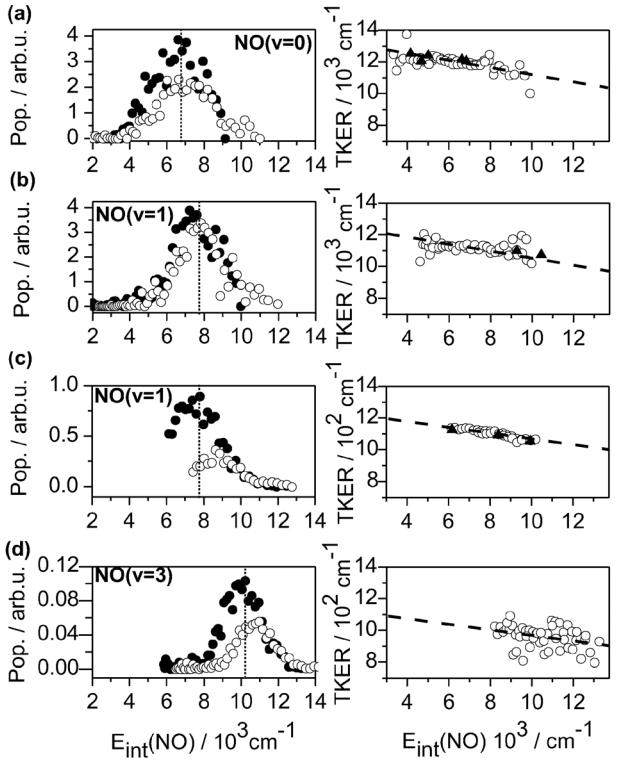

Fig. 10 Analysis of 3D-REMPI data for photolysis from S_2. The left column shows relative populations of rotational states plotted as a function of the total internal energy of the NO fragment. The vibrational state of NO(v = 0, 1, 3) monitored is indicated in each panel. Full symbols indicate populations of the $^2\Pi_{1/2}$ state, open symbols refer to the $^2\Pi_{3/2}$ state. In order to facilitate comparison of the rotational distributions, the position of the rotational states with j = 60.5 is indicated by a vertical dotted line. Panels (b) and (c) differ in the intermediate vibrational state of NO employed in the REMPI transition, and hence in the excess energy of photodissociation. The right side shows, for each of the dissociation channels of the left side, the total kinetic energy release (TKER) as a function of the total internal energy of the NO fragments.

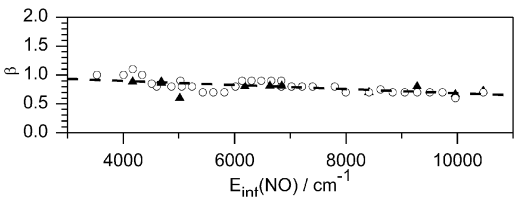

Fig. 11 Evolution of the anisotropy parameter β obtained from the VMI (triangles) and 3D-REMPI (circles) data for the rotational states of NO(v = 0) as a function of the internal energy of NO.

$v' = v''$ case. Our observation suggests that this change has a significant effect on the branching ratio into the two spin–orbit states and the various vibrational states of the NO fragment. A detailed study of this effect will require experiments in which the photolysis energy and the REMPI transition are selected independently.

The panels in the right column of Fig. 10 show that the average kinetic energies decrease linearly with rising internal energy of NO. The slope of the regression line of *ca.* 0.29 then indicates that 29% of the energy needed to populate higher rovibronic states of NO is taken from the total kinetic energy, and 71% is taken from internal degrees of freedom of the *t*-BuO counter fragment. Averaged over all rovibrational dissociation channels, 39% of the excess energy is converted to kinetic energy, whereas 23% and 38% end up as internal energies of the NO and *t*-BuO fragments, respectively.

4 Discussion

4.1 Mechanism of photodissociation

When dissociation occurs on the PES of the S_1 state, the velocity distributions for all rovibronic product states of the NO fragment show the smallest anisotropy parameter possible, $\beta = -1$. This value can only occur when the orientation of the transition moment at the time of excitation and the velocity vector of the fragments are mutually perpendicular. Since the S_1 state has nπ^* character, the transition dipole from the S_0 state is perpendicular to the plane defined by the CONO group.[10,13,30,31] On the other hand, the velocity vector must be in this plane, so both vectors are initially perpendicular. Hence, it can safely be concluded that the molecule has no time for reorientation prior to photodissociation from the S_1 state. The excited state lifetime of $\tau(S_1) \approx 130$ fs reported from transient absorption measurements[16] should be considered an upper limit due to the finite time resolution of *ca.* 200 fs in this experiment. The room temperature gas phase spectrum as well as the ion yield spectra can be well fitted by Lorentzian line shapes. The fit finds linewidths of 530 cm^{-1} and 400 cm^{-1} for room temperature and for jet-cooled molecules, respectively. These linewidths correspond to lifetimes of 10 fs and 14 fs.

For other nitrites like CH_3ONO[20,65] a direct dissociation on a purely repulsive potential energy surface and a competition between adiabatic and non-adiabatic decays caused by a barrier along the reaction coordinate have been discussed as alternative scenarios.[8,14] In the case of *t*-BuONO the evidence from our data points towards the first alternative: regardless of the vibrational state k in the S_1 state that is initially excited, the fraction of excess energy converted to kinetic energy is almost constant at 46%. Also, the rotational population distribution of the NO fragments does not depend on k, nor does it depend on the vibrational level v monitored. In fact, it is the same whether the vibrational quantum number in the NO fragment is conserved ($v = k$) or reduced by one ($v = k - 1$). If a barrier were present, it should make a big difference for the two decay channels $v = k$ and $v = k - 1$, in particular for small values of k. The excitation of the $k = 0$ level would result in a purely adiabatic dissociation, which should be significantly different from the result expected when a non-adiabatic alternative becomes available at $k \geq 1$. We conclude that in the case of *t*-BuONO excited to the S_1 state the dissociation occurs on a purely repulsive potential energy surface without passing a barrier. There is also no evidence for any contribution of torsional modes or out-of-plane bending modes.[10,12,15,24]

Our data for the photolysis *via* the S_2 state are also in line with a fast and direct decay mechanism in accordance with ref. 13. The high anisotropy (β = 0.7–1.0), the high fraction of excess energy which is converted to kinetic energy (39%) and the rotational distributions, which show a non-statistical

population of states similar for all vibrational levels of NO, strongly support this assignment.

4.2 Rotational excitation of *t*-BuO

The ion image data yield the kinetic energies of both fragments and the internal energy of the NO fragment. If this is subtracted from the energy of the photolysis photon, the difference is the sum of the dissociation energy and the internal energy of the *t*-BuO fragment. When we assume that the dissociation energy is in the range between 12 900 cm^{-1} (calculated with ACCT basis) and 14 300 cm^{-1} (obtained from thermodynamic measurements[63]), then we must conclude that a minimum internal energy of *ca.* 8500–9900 cm^{-1} always resides in the *t*-BuO fragment upon photodissociation from S_2. For dissociation from the S_1 state the corresponding value is 1100–2500 cm^{-1}. In the following we show that a large fraction of this energy can reasonably be explained as rotational energy.

The total angular momentum is conserved during the photodissociation, and we assume that it is rather small due to cooling in the supersonic expansion. The angular momentum L_{NO} carried by the NO fragment is known from the specific REMPI transition excited for a particular ion image. This must hence be compensated by the angular momentum $L_{t\text{-BuO}}$ of the counter fragment, and the angular momentum L_{rel} associated with the relative motion of the two fragments. The latter is given by

$$L_{rel} = bmv = J_{rel}\hbar \quad (6)$$

where m and v are the mass and the velocity of the NO fragment, and b is the impact parameter. For rigid fragments, the latter is given by $b = d \sin \gamma$, where d is the initial distance between the two centers of mass of the two fragments, and γ is the angle between this distance vector and the velocity vector. In *t*-BuONO the two mass centers are near the center of the N=O double bond and very close to the tertiary carbon atom. From the ACCT optimized structure we obtain a distance $d = 2.905$ Å. A value of $\gamma = 40.8°$ is estimated if we assume the velocity vector to be parallel to the breaking N–O single bond. Treating the *t*-BuO radical as a symmetric top we obtain a rotational constant of $B = 0.165$ cm^{-1} from the ACCT optimized structure.

We begin by discussing the photodissociation on the S_2 PES. Equating the internal energy of 8500–9900 cm^{-1} with rotational energy, $E_{rot} = BJ(J + 1)$, the rotational quantum number for the *t*-BuO fragment should be in the range $J_{t\text{-BuO}} = 227$–245. For this dissociation channel the typical rotational quantum number of the NO fragment is $J_{NO} \approx 60$. Hence, the angular momentum quantum number associated with the relative motion must be in the range $170 < J_{rel} < 300$. On the other hand, the typical velocity of the NO fragment of *ca.* 2700 m s^{-1} puts an upper limit of $J_{rel} < 370$. Hence, the range $170 < J_{rel} < 300$ is accessible and corresponds to a range of $27° < \gamma < 54°$ for the angle between the velocity vector and the initial distance vector between the two centers of mass of the two fragments. The estimate of $\gamma = 40.8°$, assuming dissociation along the N–O single bond, is very close to the center of this interval. Hence, we could assign the residual internal energy that apparently cannot be redistributed onto other degrees of freedom to rotational energy of the *t*-BuO fragment. This energy is locked up in this fragment since it is required there by conservation of angular momentum.

Analyzing the residual energy in the *t*-BuO fragment of 1100–2500 cm^{-1} for dissociation from the S_1 state in the same fashion ($J_{NO} \approx 30$) yields the range $50 < J_{rel} < 150$. A typical velocity of the NO fragment of *ca.* 1800 m s^{-1} results in the upper limit of $J_{rel} < 250$. This puts the range for the angle γ as $12° < \gamma < 37°$. This does not agree quite as well with the estimate from the starting geometry, $\gamma = 40.8°$, but is still reasonable.

4.3 Semiclassical MD simulation

The estimate based on experimental data presented in the previous section is supported by a semiclassical molecular dynamics calculation on the S_2 PES. A trajectory along the dynamic reaction coordinate (DRC) is started at the optimized geometry of the ground state, *i.e.* at the Franck–Condon (FC) point. The positions and velocities of all atoms are propagated by integration of Newtons equations with forces calculated from energy gradients of a MCSCF calculation. An active space of 6 orbitals containing 8 electrons was chosen. In the limit of separated fragments these orbitals are the two degenerate p orbitals of the oxygen atom perpendicular to the threefold axis of the *t*-BuO fragment (containing 3 electrons), and the pairs of π and π* orbitals of the NO fragment (containing 5 electrons). In the limit of the bound molecule *t*-BuONO these orbitals correlate with the complete π valence space of the ONO unit as well as two bonding and one antibonding σ-orbitals along the O–N bond that is broken in the photodissociation. Smaller active spaces did not account well for the dissociation, whereas larger active spaces frequently resulted in convergence problems of the MCSCF.

Fig. 12 presents some results obtained from the analysis of this DRC trajectory. The calculation was performed in the ACCD basis with a time step of 0.1 fs and C_S symmetry imposed. The trajectory stops at 36 fs. At this time the energies of the S_2 state and the S_0 state have become almost degenerate so that the MCSCF calculation for the S_2 state alone no longer converges. Panel (a) shows the distance between the two centers of mass as a function of time. After a short acceleration phase of *ca.* 10 fs duration the two fragments separate with almost constant velocity. Correspondingly, the kinetic energies of the two fragments, shown in panel (b), quickly reach constant values of 5150 cm^{-1} for the *t*-BuO fragment and 12 580 cm^{-1} for the NO fragment. The latter value corresponds to a velocity of 3170 m s^{-1}. Panel (c) shows the development of the angular momenta along the trajectory. At $t > 20$ fs the angular momentum of NO (dotted line) has reached a constant value of 75 $\hbar$-units, corresponding to a rotational energy of 9540 cm^{-1}. This is in good agreement with the maximum of the rotational distribution observed at $J \approx 60$. The angular momentum of the *t*-BuO fragment saturates at 175 $\hbar$-units, corresponding to a rotational energy of 5050 cm^{-1}. The potential energy difference between the FC point and the end of the trajectory amounts to 37 120 cm^{-1},

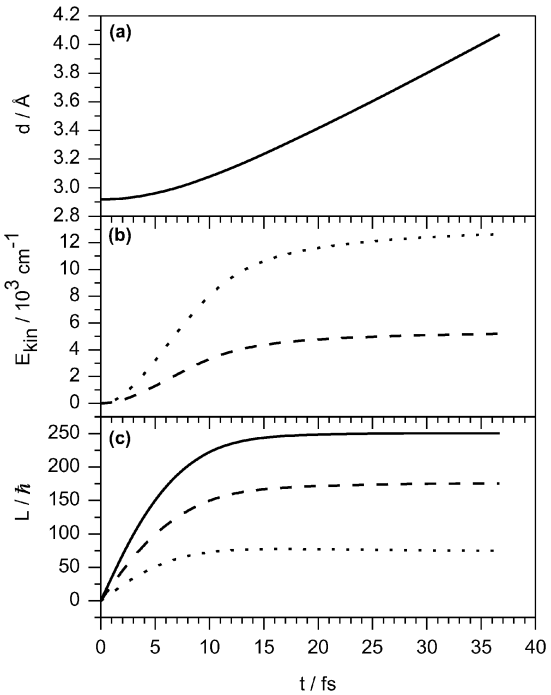

Fig. 12 Dynamic reaction coordinate on the S_2 potential energy surface. (a) Distance between the two centers of mass of the two fragments, (b) kinetic energy of both fragments, (c) angular momenta in units of $\hbar$. Dotted and dashed lines refer to the NO and *t*-BuO fragment, respectively. Full lines refer to the relative motion of both fragments.

which is the total kinetic energy of all atoms. Subtracting the kinetic energies in the center of mass movements and the rotations of both fragments from the total kinetic energy of all atoms, 4800 cm^{-1} are left that may be attributed to vibrations. An estimate of the available excess energy of the dissociation can be obtained as the difference between the energies of the system at the Franck–Condon point and at the relaxed geometry at large separation of the two fragments. With the CAS(8|6)/aug-cc-pVDZ wavefunction this estimate is 40 640 cm^{-1}. At the end of the DRC trajectory approximately 3520 cm^{-1} of energy remain as potential energy in the two fragments. We conclude that this semiclassical model, in spite of the rather approximative character, yields good agreement with experimental facts. The available excess energy is overestimated by about 30%, but the partitioning of this energy into the kinetic energy (43.6%), rotational energy (35.9%), and vibrational energy (20.5%) is very similar to experimental observation. If we attribute the vibrational energy mostly to the *t*-BuO fragment, the model finds *ca.* 33% of the excess energy as internal energy of this fragment. The experimental excess energy, $h\nu - D_0$, is in the range 30 100–31 500 cm^{-1}, depending on the choice made for the dissociation energy. A fraction of 33% of this, *i.e.* 9900–10 400 cm^{-1}, corresponds well to the experimental estimate of 8500–9900 cm^{-1}.

5 Conclusion

This paper presents the first study of the photodissociation of an aliphatic nitrite R-ONO by means of VMI and 3D-REMPI spectroscopy, with the particular example of *t*-BuONO. By careful control of the experimental conditions the contribution of clusters to the molecular beam could be completely eliminated. The presence of such clusters has led to ambiguities and misinterpretations in previous LIF studies on this and other nitrites.[8,14,18]

Photoexcitation of *t*-BuONO to the first excited singlet state leads to NO($\tilde{X}^2\Pi_\Omega$) fragments along a purely repulsive PES with planar geometry. The counter fragment is formed in its electronic ($\tilde{X}^2$E) ground state. The population of the rotational states is identical for excitation in all bands of the pronounced progression of the $S_1 \leftarrow S_0$ transition, and for all vibrational levels *v* of the NO fragment monitored. In some cases we observe a small preference for the NO($^2\Pi_{1/2}$) spin–orbit state.

The photodissociation following excitation to the second absorption band around 225 nm also occurs along a purely repulsive potential energy surface, with a planar geometry of the CONO chromophore. This is in accordance with previous studies[8,10,12,30,31] by absorption spectroscopy and LIF both in bulb and molecular beams. The majority of the NO fragments is formed in the $v = 0$ and $v = 1$ vibrational states with a maximum of the rotational populations near $j = 59.5$. No evidence for a second dissociation pathway *via* a linear ONO-transition state as postulated by Castle *et al.*[18] is found.

Acknowledgements

We are much indebted to Torsten Obernhuber who built the first VMI apparatus in our laboratory and made exploratory measurements on *t*-BuONO in 2004. A. M. Wenge gratefully acknowledges a postdoctoral fellowship from the Marie Curie Initial Training Network ICONIC (contract agreement no. 238671) under the Seventh Framework Programme of the European Union.

References

1 F. Lahmani, C. Lardeux and D. Solgadi, *J. Chem. Phys.*, 1980, **73**, 4433–4438.
2 O. Benoist D'azy, F. Lahmani, C. Lardeux and D. Solgadi, *Chem. Phys.*, 1985, **94**, 247–256.
3 F. Lahmani, C. Lardeux and D. Solgadi, *Chem. Phys. Lett.*, 1986, **129**, 24–30.
4 M. R. S. McCoustra, M. Hippler and J. Pfab, *Chem. Phys. Lett.*, 1992, **200**, 451–458.
5 A. Untch, K. Weide and R. Schinke, *Chem. Phys. Lett.*, 1991, **180**, 265–270.
6 D. S. King and J. C. Stephenson, *J. Chem. Phys.*, 1985, **82**, 2236–2239.
7 U. Brühlmann and J. R. Huber, *Chem. Phys. Lett.*, 1988, **143**, 199–203.
8 M. Hippler, F. A. H. Al-Janabi and J. Pfab, *Chem. Phys. Lett.*, 1992, **192**, 173–178.
9 D. Schwartz-Lavi, I. Bar and S. Rosenwaks, *Chem. Phys. Lett.*, 1984, **109**, 296–300.
10 D. Schwartz-Lavi, I. Bar and S. Rosenwaks, *Chem. Phys. Lett.*, 1986, **128**, 123–126.
11 R. Lavi, I. Bar and S. Rosenwaks, *J. Chem. Phys.*, 1987, **86**, 1639–1640.
12 D. Schwartz-Lavi and S. Rosenwaks, *J. Chem. Phys.*, 1988, **88**, 6922–6930.
13 C. S. Effenhauser, P. Felder and J. R. Huber, *J. Phys. Chem.*, 1990, **94**, 296–301.

14 E. Kades, M. Rösslein, U. Brühlmann and J. R. Huber, *J. Phys. Chem.*, 1993, **97**, 989–996.
15 E. Kades, M. Rösslein and J. R. Huber, *J. Phys. Chem.*, 1994, **98**, 13556–13562.
16 J. M. Mestdagh, M. Berdah, I. Dimicoli, M. Mons, P. Meynadier, P. d'Oliveira, F. Piuzzi, J. P. Visticot, C. Jouvet, C. Lardeux-Dedonder, S. Martrenchard-Barra, B. Soep and D. Solgadi, *J. Chem. Phys.*, 1995, **103**, 1013–1023.
17 H. Finke, H. Spiecker and P. Andresen, *J. Chem. Phys.*, 1999, **110**, 4777–4782.
18 K. J. Castle, J. Abbott, X. Peng and W. Kong, *Chem. Phys. Lett.*, 2000, **318**, 565–570.
19 K. J. Castle and W. Kong, *J. Chem. Phys.*, 2000, **112**, 10156–10161.
20 R. Schinke, *Photodissociation Dynamics: Spectroscopy and Fragmentation of Small Polyatomic Molecules I*, Cambridge University Press, 1993.
21 X.-F. Yue, J.-L. Sun, H.-M. Yin, Q. Wei and K.-L. Han, *J. Phys. Chem. A*, 2009, **113**, 3303–3310.
22 A. Schmaunz, U. Kensy, A. Slenczka and B. Dick, *Phys. Chem. Chem. Phys.*, 2009, **11**, 7115–7119.
23 A. Schmaunz, U. Kensy, A. Slenczka and B. Dick, *J. Phys. Chem. A*, 2010, **114**, 9948–9962.
24 R. Lavi, D. Schwartz-Lavi, I. Bar and S. Rosenwaks, *J. Phys. Chem.*, 1987, **91**, 5398–5402.
25 J. August, M. Brouard, M. P. Docker, C. J. Milne, J. P. Simons, R. Lavi, S. Rosenwaks and D. Schwartz-Lavi, *J. Phys. Chem.*, 1988, **92**, 5485–5491.
26 B. A. Keller, P. Felder and J. R. Huber, *Chem. Phys. Lett.*, 1986, **124**, 135–139.
27 D. W. Chandler and P. L. Houston, *J. Chem. Phys.*, 1987, **87**, 1445–1447.
28 A. T. J. B. Eppink and D. H. Parker, *Rev. Sci. Instrum.*, 1997, **68**, 3477–3484.
29 J. G. Calvert and J. N. Pitts, *Photochemistry*, Wiley, New York, 1967.
30 P. Tarte, *J. Chem. Phys.*, 1952, **20**, 1570–1575.
31 R. Vasudev, R. N. Zare and R. N. Dixon, *J. Chem. Phys.*, 1984, **80**, 4863–4878.
32 P. Farmanara, V. Stert and W. Radloff, *Chem. Phys. Lett.*, 1999, **303**, 521–525.
33 J. M. Engert and B. Dick, *Chem. Phys. Lett.*, 1999, **299**, 423–429.
34 P. Felder, T. K. Ha, A. M. Dwivedi and H. H. Günthard, *Spectrochim. Acta, Part A*, 1981, **37**, 337–345.
35 B. A. Keller, P. Felder and J. R. Huber, *J. Phys. Chem.*, 1987, **91**, 1114–1120.
36 P. Felder and H. H. Guenthard, *Chem. Phys. Lett.*, 1979, **66**, 283–286.
37 E. Kades, M. Roesslein and J. R. Huber, *Chem. Phys. Lett.*, 1993, **209**, 275–280.
38 S. A. Reid, J. T. Brandon and H. Reisler, *Chem. Phys. Lett.*, 1993, **209**, 22–28.
39 T. J. Obernhuber, *Setup of a Velocity-Map Ion-Imaging apparatus and measurements on the photodissociation of nitrosobenzene and* t-*butyl nitrite*, *PhD thesis*, Universität Regensburg, 2004.
40 H. W. Thompson and F. S. Dainton, *Trans. Faraday Soc.*, 1937, **33**, 1546–1555.
41 T. J. Obernhuber, U. Kensy and B. Dick, *Phys. Chem. Chem. Phys.*, 2003, **5**, 2799–2806.
42 E. Wrede, S. Laubach, S. Schulenburg, A. Brown, E. R. Wouters, A. J. Orr-Ewing and M. N. R. Ashfold, *J. Chem. Phys.*, 2001, **114**, 2629–2646.
43 R. N. Bracewell, *The Fourier Transform and its Applications*, McGraw-Hill, New York, 1978.
44 J. Winterhalter, D. Maier, J. Honerkamp, V. Schyja and H. Helm, *J. Chem. Phys.*, 1999, **110**, 11187–11196.
45 M. J. J. Vrakking, *Rev. Sci. Instrum.*, 2001, **72**, 4084–4089.
46 L. M. Smith, D. R. Keefer and S. I. Sudharsanan, *J. Quant. Spectrosc. Radiat. Transfer*, 1988, **39**, 367–373.
47 S. Manzhos and H.-P. Loock, *Comput. Phys. Commun.*, 2003, **154**, 76–87.
48 G. A. Garcia, L. Nahon and I. Powis, *Rev. Sci. Instrum.*, 2004, **75**, 4989–4996.
49 V. Dribinski, A. Ossadtchi, V. A. Mandelshtam and H. Reisler, *Rev. Sci. Instrum.*, 2002, **73**, 2634–2642.
50 C. J. Dasch, *Appl. Opt.*, 1992, **31**, 1146–1152.
51 C. Bordas, F. Paulig, H. Helm and D. L. Huestis, *Rev. Sci. Instrum.*, 1996, **67**, 2257–2268.
52 A. M. Wenge, U. Kensy and B. Dick, *Phys. Chem. Chem. Phys.*, 2010, **12**, 4644–4655.
53 G. Pretzler, H. Jäger, T. Neger, H. Philipp and J. Woisetschläger, *Z. Naturforsch.*, 1992, **47a**, 955–970.
54 M. W. Schmidt, K. K. Baldridge, J. A. Boatz, S. T. Elbert, M. Gordon, J. Jensen, S. Koseki, N. Matsunaga, K. A. Nguyen, S. Su, T. L. Windus, M. Dupuis and J. A. Montgomery, *J. Comput. Chem.*, 1993, **14**, 1347–1363.
55 A. A. Granovsky, *PC GAMESS version 7.1*, http://classic.chem.msu.su/gran/gamess/index.html.
56 S. H. Vosko, L. Wilk and M. Nusair, *Can. J. Phys.*, 1980, **58**, 1200–1211.
57 C. Lee, W. Yang and R. G. Parr, *Phys. Rev. B: Condens. Matter*, 1988, **37**, 785–789.
58 A. D. Becke, *J. Chem. Phys.*, 1993, **98**, 5648–5652.
59 F. B. van Duijneveldt, J. G. C. M. van Duijneveldt-van de Rijdt and J. H. van Lenthe, *Chem. Rev. (Washington, DC, U. S.)*, 1994, **94**, 1873–1885.
60 R. A. Kendall, T. H. J. Dunning and R. J. Harrison, *J. Chem. Phys.*, 1992, **96**, 6796–6806.
61 A. J. Barnes, H. E. Hallam, S. Waring and J. R. Armstrong, *J. Chem. Soc., Faraday Trans. 2*, 1976, **72**, 1–10.
62 *Atomic and Molecular Beam Methods*, ed. G. Scoles, Oxford University Press, 1988.
63 L. Batt and R. T. Milne, *Int. J. Chem. Kinet.*, 1976, **8**, 59–84.
64 Y. Ralchenko, A. E. Kramida, J. Reader and N. A. Team, *NIST Atomic Spectra Database (Version 3.1.5)*, 2009.
65 R. Schinke, S. Hennig, A. Untch, M. Nonella and J. R. Huber, *J. Chem. Phys.*, 1989, **91**, 2016–2029.